First Observation of $\Lambda\pi^+$ and $\Lambda\pi^-$ Signals near the $\bar{K}N(I=1)$ Mass Threshold in $\Lambda_c^+ \to \Lambda\pi^+\pi^+\pi^-$ Decay

Y. Ma, J. Yelton, K. Tanida, I. Adachi, J. K. Ahn, H. Aihara, S. Al Said, D. M. Asner, H. Atmacan,
T. Aushev, R. Ayad, V. Babu, S. Bahinipati, Sw. Banerjee, P. Behera, K. Belous, J. Bennett, M. Bessner,
B. Bhuyan, T. Bilka, D. Biswas, A. Bobrov, D. Bodrov, J. Borah, A. Bozek, M. Bračko, P. Branchini,
T. E. Browder, A. Budano, M. Campajola, D. Červenkov, M.-C. Chang, A. Chen, B. G. Cheon, K. Chilikin,
H. E. Cho, K. Cho, S.-J. Cho, S.-K. Choi, Y. Choi, S. Choudhury, D. Cinabro, S. Das, G. De Nardo,
G. De Pietro, R. Dhamija, F. Di Capua, J. Dingfelder, Z. Doležal, T. V. Dong, D. Epifanov, T. Ferber,
D. Ferlewicz, B. G. Fulsom, R. Garg, V. Gaur, A. Garmash, A. Giri, P. Goldenzweig, B. Golob, E. Graziani,
K. Gudkova, C. Hadjivasiliou, S. Halder, K. Hayasaka, H. Hayashii, M. T. Hedges, W.-S. Hou, C.-L. Hsu,
K. Inami, N. Ipsita, A. Ishikawa, R. Itoh, M. Iwasaki, W. W. Jacobs, E.-J. Jang, S. Jia, Y. Jin,
A. B. Kaliyar, K. H. Kang, T. Kawasaki, C. Kiesling, C. H. Kim, D. Y. Kim, Y.-K. Kim, K. Kinoshita,
P. Kodyš, A. Korobov, S. Korpar, E. Kovalenko, P. Križan, P. Krokovny, R. Kumar, K. Kumara,
Y.-J. Kwon, T. Lam, J. S. Lange, S. C. Lee, P. Lewis, L. K. Li, Y. Li, L. Li Gioi, J. Libby, K. Lieret,
Y.-R. Lin, D. Liventsev, T. Luo, M. Masuda, T. Matsuda, D. Matvienko, S. K. Maurya, F. Meier,
M. Merola, F. Metzner, K. Miyabayashi, G. B. Mohanty, R. Mussa, I. Nakamura, T. Nakano, M. Nakao,
Z. Natkaniec, A. Natochii, L. Nayak, M. Nayak, N. K. Nisar, S. Nishida, S. Ogawa, H. Ono, P. Oskin,
P. Pakhlov, G. Pakhlova, S. Pardi, H. Park, J. Park, S. Patra, S. Paul, R. Pestotnik, L. E. Piilonen,
T. Podobnik, E. Prencipe, M. T. Prim, A. Rostomyan, N. Rout, G. Russo, S. Sandilya, L. Santelj,
V. Savinov, G. Schnell, J. Schueler, C. Schwanda, Y. Seino, K. Senyo, M. E. Sevior, W. Shan, M. Shapkin,
C. Sharma, C. P. Shen, J.-G. Shiu, F. Simon, A. Sokolov, E. Solovieva, M. Starič, M. Sumihama,
T. Sumiyoshi, W. Sutcliffe, M. Takizawa, U. Tamponi, F. Tenchini, M. Uchida, S. Uehara, T. Uglov,
Y. Unno, K. Uno, S. Uno, P. Urquijo, Y. Usov, S. E. Vahsen, R. van Tonder, G. Varner, A. Vinokurova,
A. Vossen, D. Wang, M.-Z. Wang, M. Watanabe, S. Watanuki, O. Werbycka, E. Won, X. Xu,
B. D. Yabsley, W. Yan, S. B. Yang, J. H. Yin, C. Z. Yuan, L. Yuan, Z. P. Zhang, V. Zhilich, and V. Zhukova

(Belle Collaboration)

Using the data sample of 980 fb^{-1} collected with the Belle detector operating at the KEKB asymmetric-energy e^+e^- collider, we present the results of an investigation of the $\Lambda\pi^+$ and $\Lambda\pi^-$ invariant mass distributions looking for substructure in the decay $\Lambda_c^+ \to \Lambda\pi^+\pi^+\pi^-$. We find a significant signal in each mass distribution. When interpreted as resonances, we find for the $\Lambda\pi^+$ ($\Lambda\pi^-$) combination a mass of $1434.3 \pm 0.6(\mathrm{stat}) \pm 0.9(\mathrm{syst})$ MeV/c^2 [$1438.5 \pm 0.9(\mathrm{stat}) \pm 2.5(\mathrm{syst})$ MeV/c^2], an intrinsic width of $11.5 \pm 2.8(\mathrm{stat}) \pm 5.3(\mathrm{syst})$ MeV/c^2 [$33.0 \pm 7.5(\mathrm{stat}) \pm 23.6(\mathrm{syst})$ MeV/c^2] with a significance of 7.5σ (6.2σ). As these two signals are very close to the $\bar{K}N$ threshold, we also investigate the possibility of a $\bar{K}N$ cusp, and find that we cannot discriminate between these two interpretations due to the limited size of the data sample.

Hyperon spectroscopy near the $\bar{K}N$ threshold has been a source of excitement for more than half a century. There

are many different scenarios that can generate states in this mass region. The interplay of these scenarios makes the hyperon spectroscopy in this mass region particularly interesting. A typical example is the $\Lambda(1405)(I=0)$ state, which has been interpreted as an orbitally excited quark-diquark [1], or as a $\bar{K}N$ bound state [2]. On the other hand, the only known $I=1$ state in this mass region is the $\Sigma(1385)$. The standard quark model does not predict any
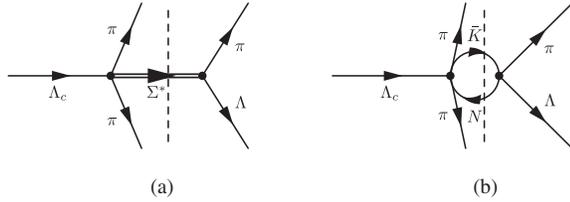
FIG. 1. $\Lambda_c^+ \rightarrow \Lambda\pi^+\pi^-\pi^+$ decay as a virtual $\Lambda - \pi$ collider. The left side of the dashed line for both (a) and (b) contains an unknown Λ_c decay form factor; the right side of the dashed line can be used to search for Σ^* resonances (a) and study $\bar{K}N$ (re-)scattering with a cusp (b), respectively.
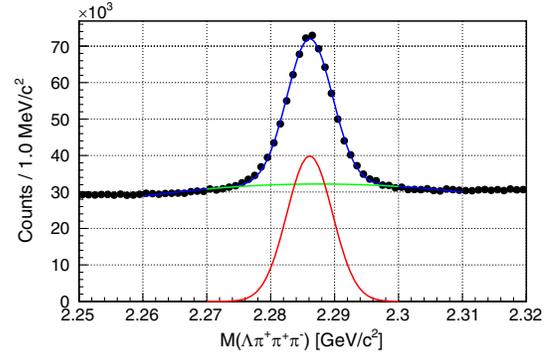

FIG. 2. The invariant mass of the $\Lambda\pi^+\pi^+\pi^-$ system after event selection. The green, red, and blue curves represent the background, signal, and total fit function, respectively. See text for details.

more states near the $\Lambda(1405)$ mass, so if a Σ^* resonance is observed, it may be exotic. The $\bar{K}N(I = 1)$ interaction is, most likely, not strong enough to produce a bound state, but a virtual state could exist [3] and could be observed as a threshold cusp. The shape of such a cusp reflects the scattering length of the $\bar{K}N(I = 1)$ interaction, which is particularly interesting in relation with kaon condensation in neutron stars, where K^-n interaction is most important.

In this Letter we report a study of $\Lambda\pi^+$ and $\Lambda\pi^-$ invariant mass distributions in the region above the $\Sigma(1385)$, in the decay $\Lambda_c^+ \rightarrow \Lambda\pi^+\pi^+\pi^-$. The charge conjugate mode is implied throughout the current Letter. Heavy baryon (Λ_c^+) decay provides a unique chance to investigate hyperon spectroscopy. In particular, study of the $[\Lambda\pi^{\pm}]$ pair in the decay $\Lambda_c^+ \rightarrow [\Lambda\pi^{\pm}]\pi^{\mp}\pi^+$ provides data comparable to a $\Lambda - \pi$ collider in the range of 0 to 0.7 GeV/c^2 above the $\Lambda\pi^{\pm}$ mass threshold. This allows analysis of the $I = 1$, $S = -1$ sector to be performed in this range. In the present analysis, as shown in Fig. 1, we consider possible Σ^* resonances, and a $\bar{K}N$ threshold cusp.

Our data sample corresponds to the 980 fb^{-1} integrated luminosity collected with the Belle detector at the KEKB asymmetric-energy e^+e^- collider [4]. Most of the data are taken at the $\Upsilon(nS)(n = 1$–5) resonances together with a small integrated luminosity collected off resonance. Belle detector is a large-solid-angle magnetic spectrometer consisting of a silicon vertex detector (SVD), a 50-layer central drift chamber (CDC), an array of aerogel threshold Cherenkov counters (ACC), a barrel-like arrangement of time-of-flight scintillation counters (TOF), and an electromagnetic calorimeter made of CsI(Tl) crystals (ECL). These components are surrounded by a superconducting solenoid with a 1.5 T magnetic field. The details of the Belle detector can be found in [5].

We use a set of Monte Carlo simulation tools to optimize the event selections. Event generation uses the EVTGEN [6] package and GEANT3 is used for Belle detector response simulation [7]. The event reconstruction starts with charged hadron (h) identification to select p and $\pi^{\pm}$. For each charged track, a likelihood $[\mathcal{L}(h)]$ of particle identification (PID) is assigned based on the measurement with CDC, TOF, and ACC [8]. The ratio of the PID likelihoods,

$\mathcal{R}(h_S\colon h_B) = \mathcal{L}(h_S)/[\mathcal{L}(h_S) + \mathcal{L}(h_B)]$, is used for event selection. Only $\pi^{\pm}$ with $\mathcal{R}(\pi\colon K) > 0.2$ and $\mathcal{R}(\pi\colon p) > 0.4$ and p with $\mathcal{R}(p\colon\pi) > 0.6$ are used in the following data analysis. The PID efficiency is approximately 99% for $\pi^{\pm}$ and 91% for proton, respectively. The kinetic information of the $\pi^{\pm}$ and p obtained from the tracking device (SVD and CDC) are used to reconstruct Λ and Λ_c^+. During the reconstruction, daughter particles of the corresponding decay are fitted to the common vertex with the mass of the mother particle as a mass-constraint vertex fit. The so reconstructed Λ trajectory is used for the Λ_c^+ reconstruction. A confidence level > 0.001 is required to select good Λ and Λ_c^+ candidates. To optimize the signal to noise ratio (S/N) of the final $[\Lambda\pi^{\pm}]$ spectrum, we require the scaled momentum of Λ_c^+ to satisfy $x_p = pc/\sqrt{s/4 - M_{\Lambda_c^+}^2 c^4} > 0.43$, where p is the reconstructed Λ_c^+ momentum in the center-of-mass frame, c is the speed of light, s is the square of the center-of-mass energy and $M_{\Lambda_c^+}$ is the mass of Λ_c^+. A mass window of $\Delta M \leq 8$ MeV/c^2 centered at the Λ_c^+ nominal mass corresponding to $\pm 2.1\sigma$ of Λ_c^+ signal is also applied [9]. The Λ_c^+ decay vertex is required to satisfy $dr < 0.2$ cm and $dz < 2$ cm, where dr and dz are the distance from the interaction point transverse to, and along, the e^+ beam direction. In addition, to further improve the signal sensitivity in the $\Lambda\pi^+$ spectrum, we veto $\Sigma(1385) \rightarrow \Lambda\pi^-$ contributions to the $\Lambda_c^+ \rightarrow \Lambda\pi^+\pi^-\pi^+$ decay with a mass window of 10 MeV centered at the nominal mass of $\Sigma(1385)^-$ [9]. This method is only effective for the $\Lambda\pi^+$ mode because of the different background level in the $\Lambda\pi^-$ mode.

The reconstructed Λ_c^+ invariant mass from $\Lambda_c^+ \rightarrow \Lambda\pi^+\pi^+\pi^-$ decay after event selection is shown in Fig. 2. The Λ_c^+ invariant mass is fitted with a second order Chebyshev polynomial for background and a Gaussian function for signal. The fitted Λ_c^+ invariant mass in our data analysis is 2286.12 ± 0.01 and 0.34 ± 0.14 MeV/c^2 lower than the world average value, where the uncertainty is
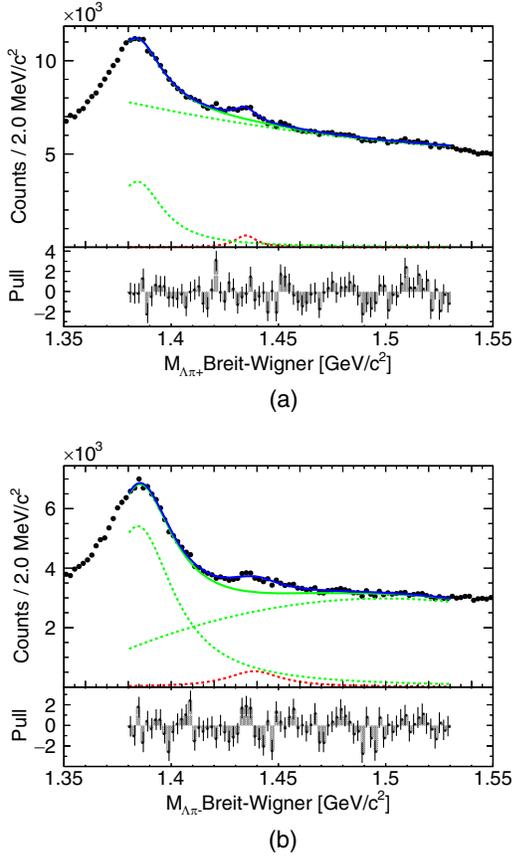
FIG. 3. $\Lambda\pi^+$ (a) and $\Lambda\pi^-$ (b) invariant mass distribution fitted with a Breit-Wigner signal and a background function. The solid (dotted) green, red, and blue curves represent the (breakdown) background, signal, and total fit function, respectively. Fitting range: 1.380–1.530 GeV/c^2. See text for details.

dominated by the reference value [9]. We consider this -0.34 MeV/c^2 shift as the absolute Belle energy scale uncertainty and will use it to estimate the systematic uncertainty for the $\Lambda\pi$ invariant mass.

The [$\Lambda\pi^\pm$] invariant mass resolution is obtained by simulation and parametrized as a sum of two Gaussian functions with $\sigma_1 = 1.15$ MeV/c^2, $\sigma_2 = 2.52$ MeV/c^2, an area ratio of 3.5, and a common mean. The systematic uncertainty for the resolution function is estimated by comparing the reconstructed Λ_c^+ invariant mass from simulation and Belle data. The simulated resolution is ∼4% wider than the data, which will be used to evaluate the systematic uncertainty in our data analysis. In the following data analysis, the resolution function is convoluted with the signal functions Eq. (1) and Eq. (2) to derive the fit parameters of interest.

The reconstructed [$\Lambda\pi^\pm$] invariant mass spectrum from $\Lambda_c^+ \to [\Lambda\pi^\pm]\pi^\mp\pi^+$ decay after all event selections is shown in Figs. 3 and 4 for two different fitting models as will be explained in the text. The reconstruction efficiency is evaluated to be ∼8% based on simulation.

Clear enhancements near the $\bar{K}N$ mass thresholds are observed in the $\Lambda\pi^+$ and $\Lambda\pi^-$ invariant mass spectrum, respectively. We have confirmed that these enhancements originate from Λ_c^+ decays by comparing the $\Lambda\pi^\pm$ invariant mass spectrum from the Λ_c^+ mass window and the side band regions centered at Λ_c^+ nominal mass $\pm5\sigma$ with $\pm1.1\sigma$ width.

We investigate the signals using two different parametrizations of the signal shape: a Breit-Wigner function which describes a Σ^* resonance, and the Dalitz model [10] which describes a $\bar{K}N$ cusp. A common background function for both $\Lambda\pi^\pm$ charge modes is used. It consists of two components: a Breit-Wigner function for the $\Sigma(1385)^\pm$ contribution and a second-order Chebyshev polynomial function for the high-mass background events. Five free parameters, i.e., relative yield between these two components, peak and width of the Breit-Wigner function, and two coefficients of the Chebyshev polynomial function are used for the fit.

To interpret the signals as Σ^* resonances, we use a nonrelativistic Breit-Wigner function defined as

$$f_{\text{BW}} = \frac{\Gamma/2}{(E - E_{\text{BW}})^2 + \Gamma^2/4}, \tag{1}$$

where E is the $\Lambda\pi^\pm$ invariant mass, E_{BW} is the Σ^* mass, and Γ is the resonance width. A binned least-χ^2 fit to the spectrum is shown in Fig. 3 and the fit results are summarized in Table I.

Given the overlap of the observed signals and the $\bar{K}N$ mass threshold, it is natural to expect a strong $\bar{K}N$ contribution via $\bar{K}$-N rescattering as illustrated in Fig. 1(b). In particular, by neglecting the Λ_c^+ decay form factor, the $\bar{K}N$ cusp can be related to the $\bar{K}$-N complex scattering length ($A = a + ib$) with the Dalitz model [10]:

$$f_D = \frac{4\pi b}{(1 + kb)^2 + (ka)^2}, \qquad E > m_{\bar{K}N}$$

$$= \frac{4\pi b}{(1 + \kappa a)^2 + (\kappa b)^2}, \qquad E < m_{\bar{K}N}, \tag{2}$$

where k and κ are the magnitude of the $\bar{K}N$ relative momentum above and below threshold, respectively. Specifically, $k = \sqrt{2\mu(E - m_{\bar{K}N})}$ for $E > m_{\bar{K}N}$ and $\kappa = \sqrt{2\mu(m_{\bar{K}N} - E)}$ for $E < m_{\bar{K}N}$, where $\mu = 1/(1/m_N + 1/m_{\bar{K}})$ is the reduced mass of the $\bar{K}N$ system.

TABLE I. Breit-Wigner fitting results. The quoted errors are statistical only.

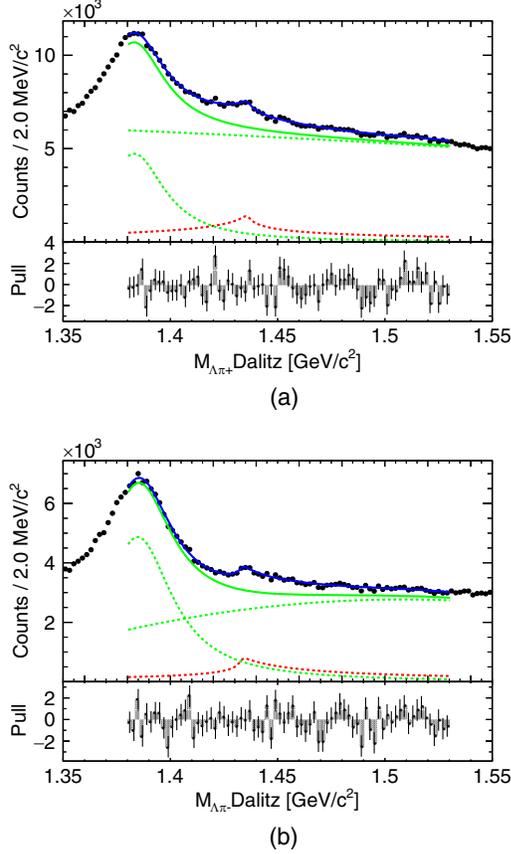| Mode	E_{BW} (MeV/c^2)	Γ (MeV/c^2)	χ^2/NDF
$\Lambda\pi^+$	1434.3 ± 0.6	11.5 ± 2.8	74.4/68
$\Lambda\pi^-$	1438.5 ± 0.9	33.0 ± 7.5	92.3/68

FIG. 4. $\Lambda\pi^+$ (a) and $\Lambda\pi^-$ (b) invariant mass distribution fitted with the Dalitz model for the signal and a background function. The solid (dotted) green, red, and blue curves represent the (breakdown) background, signal, and total fit function, respectively. Fitting range: $1.380 \sim 1.530$ GeV/c^2. See text for details.

Figure 4 shows the fit result with the Dalitz model by using binned least-χ^2 method. The obtained scattering length is given in Table II. The quoted uncertainties are statistical only.

To test the interpretation of the observed signal as $\bar{K}N$ cusps, we adopt the Flatté parametrization given in [11]:

$$f_{\mathrm{Fl}} = \frac{\Gamma}{(E - m_{\bar{K}N} - E_{\mathrm{BW}})^2 + (\Gamma + gk)^2/4}, \qquad E > m_{\bar{K}N}$$

$$= \frac{\Gamma}{(E - m_{\bar{K}N} - E_{\mathrm{BW}} - g\kappa/2)^2 + \Gamma^2/4}, \qquad E < m_{\bar{K}N},$$

$$(3)$$

TABLE II.   Dalitz model fitting results.

Mode	a (fm)	b (fm)	χ^2/NDF
$\Lambda\pi^+$	0.48 ± 0.32	1.22 ± 0.83	68.9/68
$\Lambda\pi^-$	1.24 ± 0.57	0.18 ± 0.13	78.1/68

where E, E_{BW}, and Γ have the same definition as in Eq. (1), g is the coupling constant to $\bar{K}N$, and k (κ) is the magnitude of the $\bar{K}N$ relative momentum above (below) threshold as defined in Eq. (2). However, it is known that the three parameters (E_{BW}, Γ, and g) in Flatté parametrization are not independent, but are correlated by the so-called scaling behavior [11].

The scaling behavior suggests that by fixing E_{BW} far away from the $\bar{K}N$ mass threshold ($\sim$1.435 GeV/c^2), the Flatté parametrization effectively describes a cusp. This can be made explicit with the help of the effective range expansion, which relates the Flatté parametrization to the scattering lengths as [11]

$$A = a + ib = \frac{g}{2(E_{\mathrm{BW}} - i\Gamma/2)}. \qquad (4)$$

This relation is based on the process of $\bar{K}$-N rescattering into the $\Lambda\pi$ final state as illustrated in Fig. 1(b). In particular, we can customize the Flatté parametrization by replacing $\Gamma = 2E_{\mathrm{BW}}b/a$, $g = 2E_{\mathrm{BW}}(a + b^2/a)/\hbar c$, and set an arbitrarily large E_{BW} (10 GeV was used in this analysis). The scattering length derived this way is largely consistent with the Dalitz model. The difference is summarized in Table IV as a systematic uncertainty.

In the Breit-Wigner fit, three types of systematic uncertainties are considered: uncertainty due to the absolute Belle energy scale, uncertainty induced by the resolution function, and uncertainty due to the fitting procedure. The absolute Belle energy scale is estimated to be 0.34 MeV/c^2 lower than the reference value as previously described. We therefore shift the $\Lambda\pi^\pm$ invariant mass spectrum by +0.34 MeV/c^2 to derive the systematic uncertainty. The uncertainty induced by the resolution function is checked by shrinking the resolution by 4%, which is obtained by comparing Λ_c^+ mass distribution between simulation and data as mentioned before. To evaluate the uncertainty due to the fitting procedure, we define a new background function

TABLE III.   Systematic uncertainties for the Breit-Wigner fitting parameters in [MeV].

Source	Mode	E_{BW} (MeV/c^2)	Γ (MeV/c^2)
Energy scale	$\Lambda\pi^+$	+0.5	−0.1
Resolution	$\Lambda\pi^+$	0.0	+0.1
Fitting procedure	$\Lambda\pi^+$	+0.8	−5.3
Total	$\Lambda\pi^+$	$+0.9 \atop -0.0$	$+0.1 \atop -5.3$
Final value		± 0.9	± 5.3
Energy scale	$\Lambda\pi^-$	+0.2	−2.9
Resolution	$\Lambda\pi^-$	0.0	+0.1
Fitting procedure	$\Lambda\pi^-$	−2.5	−23.4
Total	$\Lambda\pi^-$	$+0.2 \atop -2.5$	$+0.1 \atop -23.6$
Final value		± 2.5	± 23.6

TABLE IV. Systematic uncertainties for the Dalitz fitting parameters in [fm].

Source	Mode	a (fm)	b (fm)
Energy scale	$\Lambda\pi^+$	+0.03	−0.17
Resolution	$\Lambda\pi^+$	−0.01	−0.03
Fitting procedure	$\Lambda\pi^+$	+0.37	+2.54
Model	$\Lambda\pi^+$	+0.05	−0.05
Total	$\Lambda\pi^+$	$+0.38$ -0.01	$+2.54$ -0.18
Final value		±0.38	±2.54
Energy scale	$\Lambda\pi^-$	+0.19	−0.10
Resolution	$\Lambda\pi^-$	−0.01	0.00
Fitting procedure	$\Lambda\pi^-$	+1.55	−0.17
Model	$\Lambda\pi^-$	−0.16	−0.05
Total	$\Lambda\pi^-$	$+1.56$ -0.16	$+0.00$ -0.20
Final value		±1.56	±0.20

as a third-order Chebyshev polynomial and change the fitting range to 1.420–1.520 GeV/c^2 for both $\Lambda\pi$ charge modes. By excluding $\Sigma(1385)^{\pm}$ from the fitting range, we estimate the uncertainty related to the $\Sigma(1385)^{\pm}$ background component. The resulting systematic uncertainties for the Breit-Wigner fitting are summarized in Table III, where the independent contributions are added in quadrature for the total. To be conservative, we take the larger value of any uncertainty that is asymmetric and use it as a symmetric uncertainty for the final result.

For the Dalitz model fit, we also consider the absolute Belle energy scale uncertainty, resolution uncertainty, and the fitting procedure uncertainty, where the same treatment as the Breit-Wigner case is used. In addition, we also include the uncertainty induced by the data fitting model, which is obtained by comparing the difference between the Dalitz model and Flatté parametrizations. The systematic uncertainties are summarized in Table IV, where the independent contributions are added in quadrature for the total. Similar to the Breit-Wigner case, we take the larger value of any uncertainty that is asymmetric and use it as a symmetric uncertainty for the final result.

The statistical significance of the signals is derived by excluding the peaks from the fit, finding the change in the log-likelihood ($\Delta[\ln(L)]$) and converting this to a p value, taking into account the change in the number of degrees in freedom. This is then converted to an effective number of standard deviations. The same treatment is applied for the two fitting procedures and for each $\Lambda\pi$ charge mode. The lowest significance out of four combinations is reported in this Letter as 7.5σ for the $\Lambda\pi^+$ mode and 6.2σ for the $\Lambda\pi^-$ mode, respectively.

To understand the $\Lambda\pi^{\pm}$ invariant mass enhancement, two interpretations as Σ^* resonances and $\bar{K}N$ threshold cusps are tested. For the Σ^* interpretation, we have the final results for $\Lambda\pi^+$ ($\Lambda\pi^-$) peak of $M = 1434.3 \pm 0.6$(stat) $\pm$ 0.9(syst) MeV/c^2 [1438.5 $\pm$ 0.9(stat) $\pm$ 2.5(syst) MeV/c^2], width = 11.5 $\pm$ 2.8(stat) $\pm$ 5.3(syst) MeV/c^2 [33.0 $\pm$ 7.5(stat) $\pm$ 23.6(syst) MeV/c^2]. It is noticeable that the $\Lambda\pi^+$ peak $E_{BW} = 1433.9 \pm 0.6$ MeV/c^2 is lower than the $\bar{K}^0 p$ mass threshold $m_{\bar{K}^0 p} = 1435.9$ MeV/c^2 and the $\Lambda\pi^-$ peak $E_{BW} = 1437.7 \pm 0.9$ MeV/c^2 is higher than the $K^- n$ mass threshold $m_{K^- n} = 1433.2$ MeV/c^2, where the reference values for the kaon and nucleon mass are taken from world average [9].

If we interpret the signals as threshold cusps, we can derive the following scattering lengths: $\bar{K}^0$-p (K^--n) with $\Lambda\pi^+$ ($\Lambda\pi^-$) mode as $a = 0.48 \pm 0.32$(stat) ± 0.38(syst) fm [1.24 ± 0.57(stat) ± 1.56(syst) fm] and $b = 1.22 \pm 0.83$ (stat) ± 2.54(syst) fm [0.18 ± 0.13(stat) ± 0.20(syst) fm]. The scattering length derived in our data analysis is larger than the previous results [12–14]. This difference may be due to the neglected decay form factor of an order of 0.5 fm.

On the theoretical side, both interpretations are discussed, but the cusp interpretation may be more favored. Oller and Meißner discussed the possibility of a resonance in the $I = 1$ channel and reported a pole at $(1444.0 - i69.4)$ MeV in the second Riemann sheet [3]. However, the imaginary part is too large to explain the present structure. Many theories [13–15] predicted a threshold cusp in the $I = 1$ channel. In addition, Ref. [3] also reported another (virtual) pole in the third Riemann sheet below the threshold, which could produce a cusp at the threshold.

We report the first observations of $\Lambda\pi^{\pm}$ invariant mass enhancements near the $\bar{K}N$ mass thresholds in the substructure of the $\Lambda_c^+ \to \Lambda\pi^+\pi^+\pi^-$ decay. The significance for the observed signals are 7.5σ for $\Lambda\pi^+$ combination, and 6.2σ for $\Lambda\pi^-$ combination, respectively. Limited by the statistics and the shape of the background, we cannot distinguish between Σ^* resonances and $\bar{K}N$ threshold cusps, since both fits give similar χ^2s.

[1] M. Arima, S. Matsui, and K. Shimizu, Phys. Rev. C **49,** 2831 (1994).

[2] J. M. M. Hall, W. Kamleh, D. B. Leinweber, B. J. Menadue, B. J. Owen, A. W. Thomas, and R. D. Young, Phys. Rev. Lett. **114,** 132002 (2015).

[3] J. Oller and U.-G. Meißner, Phys. Lett. B **500,** 263 (2001).

[4] S. Kurokawa and E. Kikutani, Nucl. Instrum. Methods Phys. Res., Sect. A **499,** 1 (2003), and other papers included in this volume; T. Abe *et al.*, Prog. Theor. Exp. Phys. **2013,** 03A001 (2013), and references therein.

[5] A. Abashian *et al.* (Belle Collaboration), Nucl. Instrum. Methods Phys. Res., Sect. A **479,** 117 (2002); J. Brodzicka *et al.*, Prog. Theor. Exp. Phys. **2012,** 04D001 (2012).

[6] D. J. Lange, Nucl. Instrum. Methods Phys. Res., Sect. A **462,** 152 (2001).

[7] R. Brun *et al.*, CERN Report No. DD/EE/84-1, 1984.

[8] E. Nakano, Nucl. Instrum. Methods Phys. Res., Sect. A **494,** 402 (2002).

[9] R. L. Workman *et al.* (Particle Data Group), Prog. Theor. Exp. Phys. **2022,** 083C01 (2022).

[10] R. H. Dalitz and A. Deloff, Czech. J. Phys. B **32,** 1021 (1982).

[11] V. Baru, J. Haidenbauer, C. Hanhart, A. Kudryavtsev, and Ulf-G. Meißner, Eur. Phys. J. A **23,** 523 (2005).

[12] B. Borasoy, U. G. Meissner, and R. Nissler, Phys. Rev. C **74,** 055201 (2006).

[13] Y. Ikeda *et al.*, Nucl. Phys. **A881,** 98 (2012).

[14] J. Yamagata-Sekihara *et al.*, Prog. Theor. Exp. Phys. **2013,** 043D02 (2013).

[15] Y. Kamiya *et al.*, Nucl. Phys. **A954,** 41 (2016).